Available online at www.sciencedirect.com
ScienceDirect
Applied Catalysis B: Environmental 81 (2008) 236–243
APPLIED CATALYSIS B: ENVIRONMENTAL
www.elsevier.com/locate/apcatb

Preparation of mesoporous copper cerium bimetal oxides with high performance for catalytic oxidation of carbon monoxide

Jingkang Zhu, Qiuming Gao *, Zhi Chen

State Key Laboratory of High Performance Ceramics and Superfine Microstructures, Shanghai Institute of Ceramics, Graduate School, Chinese Academy of Sciences, 1295 Dingxi Road, Shanghai 200050, PR China

Received 11 June 2007; received in revised form 20 December 2007; accepted 21 December 2007
Available online 3 January 2008

Abstract

A series of mesoporous copper cerium bimetal oxides with different copper contents were replicated from the KIT-6 silica using mixed solutions of Cu(II) and Ce(III) nitrates as metal sources. These bimetal oxides were characterized by XRD, TEM, nitrogen sorption at 77 K and XPS. Catalytic oxidation of CO as a standard reaction was used to test their activities. The optimized performance was achieved for the catalyst $CuCeO_2$-20 with 20 mol% copper contents and half CO conversion was reached at 350 K with a space velocity of 260,000 mL h^{-1} g_{cat}^{-1}. No obvious deactivation was observed for over 10 h on stream at 373 K.

Keywords: Copper cerium bimetal oxide; Mesoporous; KIT-6 silica; Nanocasting; CO oxidation

1. Introduction

The reaction on catalytic carbon monoxide (CO) oxidation is very important in the field of environmental and technological applications such as automotive exhaust abatement, proton exchange membrane fuel cells (PEMFC), CO gas detection sensors and closed-cycle CO_2 pulsed lasers [1–3]. Noble metals (Pt, Pd, Rh and so forth) are well-known CO oxidation catalysts with high activity and desirable air and temperature stability. However, the relatively high cost and limited availability of these metals may inhibit their large-scale applications. Thus, design and synthesis of more cost-effective and affordable noble metal-free catalysts are of particular interest [4].

The copper cerium bimetal oxides have been demonstrated as efficient catalysts for CO oxidation with high catalytic activity even comparable with that of the commercial precious metal catalysts [4,5]. The enhanced catalytic activity of the CuO_x/CeO_2 catalysts was generally ascribed to synergistic effects in relation with high degree of interdispersion, creation of defects (e.g., oxygen vacancies) and facile redox interplay between copper and cerium redox couples (Cu^{2+}/Cu^{+} and Ce^{4+}/Ce^{3+}) [5–11]. Many procedures to prepare CuO_x/CeO_2 catalysts have been developed. Usually, the impregnation is known for the low Cu(II) loading due to the Cu(II) ions segregation and the heterogeneous coprecipitation in basic media has inherent shortcoming of inhomogeneities [12,13]. In order to improve the interdispersion and the homogeneities, other methods such as homogeneous precipitation [14–17], solution combustion [18–22], inert gas condensation (IGS) [11,23] and reverse microemulsion [7,24–26] were introduced. The CuO_x/CeO_2 nanocomposite particles synthesized via the routes mentioned above not only exhibited significantly improved catalytic properties for CO oxidation [11,27] but also demonstrated great potential applications in various reactions including NO reduction and hydrocarbon oxidation [18,24], preferential CO oxidation in H_2-rich streams (CO-PROX reaction) [14,20,28], water–gas shift [7,16,29,30] and methanol steam reforming [19], which are of high technological significance.

Recently, much attention has been attracted on nanostructures with regular shape, large surface-to-volume ratio and hollow structures, which are in close relation with their catalytic properties [31–34]. CuO-loaded CeO_2 nanorods showed outstanding catalytic activity for CO oxidation, which was attributed to the favorable synergetic effects between CuO and the definite reactive planes exposed by the ceria nanorods [31]. Mesoporous CeO_2 was synthesized recently via

* Corresponding author. Tel.: +86 21 52412513; fax: +86 21 52413122.
E-mail address: qmgao@mail.sic.ac.cn (Q. Gao).

0926-3373/$ – see front matter © 2007 Elsevier B.V. All rights reserved.
doi:10.1016/j.apcatb.2007.12.017

a nanocasting pathway using KIT-6 silica, a three-dimensionally ordered mesoporous silica exhibiting a cubic Ia3d structure, as the template. When CuO was loaded, the catalytic activities toward CO oxidation over the mesoporous CuO_x/CeO_2 catalysts were much higher than that over catalyst using ceria decomposed from the cerium nitrate hydrate as support [32]. However, since the CuO was incorporated by the wetness impregnation technique, the loading amounts of Cu(II) were low and the specific surface area diminished with the increase of the CuO loading amounts due to the block of the pore channels.

In this study, we report the preparation of mesoporous copper cerium bimetal oxides with different CuO contents in the crystalline walls via replication from KIT-6. Their specific surface areas were preserved, the catalytic activities for CO oxidation over these catalysts were optimized, and the highest activity was achieved for the catalyst $CuCeO_2$-20 with 20 mol% copper contents.

2. Experimental

2.1. Synthesis of KIT-6 Silica

The KIT-6 silica was prepared under hydrothermal conditions according to the established procedures with minor modification [35]. Typically, first, 4.0 g of triblock copolymer P123 ($EO_{20}PO_{70}EO_{20}$) and 145 mL of water was mixed and stirred at 308 K overnight. Then, 6.5 mL of 37 wt.% HCl and 4.0 g of *n*-butanol were added. The mixture was kept stirring for 2 h. After that, 8.2 g of tetraethyl orthosilicate (TEOS) was added under vigorous stirring and the mixture was kept at the same temperature for 24 h. The gel was then transferred into a stainless-steel autoclave and heated at 403 K for 3 d under static conditions. At last, the white solids were recovered by filtration, washed with deionized water and dried. Thereafter, the products were calcined in air at 823 K for 6 h at a heating rate of 2 K min^{-1}.

2.2. Preparation of mesoporous copper cerium bimetal oxides

Stock mixed solution of Cu(II) nitrate and Ce(III) nitrate was prepared by dissolving copper(II) nitrate trihydrate ($Cu(NO_3)_2{\cdot}3H_2O$) and cerium(III) nitrate hexahydrate ($Ce(NO_3)_3{\cdot}6H_2O$) in ethanol. In all cases, the concentrations of the total metal ions (i.e., [Cu(II)] + [Ce(III)]) were kept constant at 0.7 M. The molar percentage ratio of Cu(II) to total metal, $X = ([Cu(II)]/([Ce(III)] + [Cu(II)])) \times 100$, was varied between 5 and 50. The prepared mesoporous copper cerium bimetal oxides were named as $CuCeO_2$-*X*, where *X* is the nominal percentage of Cu(II). Typically, 0.2 g of KIT-6 silica was dispersed in 3.0 mL of the above ethanol solution containing stoichiometric amounts of corresponding metal salts and stirred at room temperature for 1 h. Ethanol was removed by evaporation through heating the mixture overnight at 373 K. Afterward, the resulting powder was heated in a ceramic crucible in an oven at 673 K for 6 h to completely decompose the nitrate species. The impregnation step was repeated with 2.0 mL of the metal salt solution in order to achieve higher loadings. After evaporation of the solvent, the resulting material was calcined at 823 K for 6 h. The silica template was then removed at 323 K through etching twice in 10 mL of 2.0 M NaOH aqueous solution. The mesoporous bimetal oxides were recovered by centrifugation, washed with water and finally dried at 323 K.

For comparison, mesoporous cerium dioxide was synthesized and 20 mol% CuO was loaded on this CeO_2 support according to methods previously reported [32]. The obtained catalyst was analyzed by X-ray diffraction and nitrogen sorption at 77 K, revealing the essentially similar phase composition and textural properties to that reported in the literature.

2.3. Characterization

Powder X-ray diffraction (XRD) patterns of the as-synthesized samples were recorded on a Rigaku D/Max-2200 X-ray diffractometer using Ni-filtered Cu Kα radiation ($\lambda = 0.15418$ nm; 40 kV, 40 mA). Transmission electron microscope (TEM) and high resolution TEM micrographs were obtained on a JEM-2010 electron microscope operating at 200 kV. Energy dispersive X-ray (EDX) spectra were collected from an Oxford Link ISIS EDX spectrometer attached to the field emission TEM. Nitrogen-sorption isotherms were measured at 77 K on a Micromeritics ASAP-2020M instrument under continuous adsorption conditions. Before measurements, all samples were outgassed at 383 K for 5 h under vacuum. The specific surface areas were calculated by the Brunauer–Emmett–Teller (BET) method. The pore size is defined as the position of the maximum in the pore-size distribution and calculated by the Barrett–Joyner–Halenda (BJH) method based on the adsorbed branches of the isotherms. X-ray photoelectron spectroscopy (XPS) analyses were carried out on a Microlab 310-F Scanning Auger Microprobe equipped with a 150 W (15 kV by 10 mA) aluminum Kα (1486.6 eV) anode as the X-ray source, using a pass energy of 50 eV with a step size of 0.1 eV. The samples were analyzed in the XPS chamber under an ultrahigh vacuum (10^{-7} Pa base pressure). The energy scales were calibrated with respect to the highest binding energy peak for Ce(IV) $3d_{3/2}$ at 916.7 eV.

2.4. Catalytic tests

The activities of the catalysts for CO oxidation were measured in a quartz tubular reactor (6.0 mm in inner diameter) at atmospheric pressure in a temperature range of 293–473 K. No pretreatment was applied before each catalytic test. Thirty milligrams of catalyst was supported on the glass wool in the tube with a thermocouple placed immediately. A gas mixture of 1.0 vol.% CO in air was fed at a total inlet flow rate of 130 mL min^{-1} (ambient temperature and pressure), corresponding to a space velocity of 260,000 mL h^{-1} $g_{cat}{}^{-1}$. We should mention that different masses of catalysts (30–200 mg) and flow rates (50–130 mL min^{-1}) were employed in the

catalytic measurements. When large mass of catalyst and low flow rate were used, the light-off curves for the $CuCeO_2$-X catalysts were too close to distinguish their activity sequence. It is well known that the presence of mass and heat transfer resistance may lead to underestimate the catalytic activities of catalysts for CO oxidation. In order to minimize the transfer limitations and thus differentiate the activity sequence of these catalysts, less mass of catalyst (30 mg) and relatively high flow rate (130 mL min^{-1}) were chosen in the catalytic tests. The kinetic regime was checked by varying the flow rate and mass of catalyst in the same proportion to maintain a constant weight/flow (W/F) ratio of 0.03 g s cm^{-3}. Here, the external mass transfer limitations may be eliminated. The catalytic experiments were carried out under steady state condition. Typically, the reactor was heated to the desired temperature with a rate of 2 K min^{-1} under the reagent mixture flow and then the catalytic data at this temperature were taken during 20 min after at least 0.5 h on stream. Therefore, the influence brought by the exothermic reaction can be excluded.

The concentrations of the outlet CO after stepwise changes in the reaction temperatures were analyzed with an on-line gas chromatograph (SP-6890, molecular sieves 13× column) equipped with a thermal conductivity detector (TCD). Multiple concentrations of the outlet gas were taken and averaged to ensure that the catalytic system had reached steady state. The conversion of CO was calculated using the integrated peak area differences between the CO fed initially and the effluent CO from the reactor with an accuracy of about ±5%. Temperature for 50% conversion (T_{50}) as an index was used to evaluate the activity of the catalyst.

3. Results and discussion

3.1. XRD analyses

Fig. 1A shows the wide-angle XRD patterns of the silica-free $CuCeO_2$-X (X = 5–50) replicas. For samples with copper contents in the range of 5–30%, the diffraction patterns are quite similar and all the Bragg diffraction peaks can be indexed to the face-centered cubic fluorite phase of CeO_2 (JCPDS #43-1002). Segregation of tenorite (CuO) was discerned for the $CuCeO_2$-40 in a minor way and became distinct for the $CuCeO_2$-50 sample. The absence of CuO diffraction peaks for samples with copper contents below 30% was ascribed to the substitution of copper in the ceria lattice or the formation of extremely small copper oxide clusters, indicating homogeneous dispersion of copper species on the ceria matrices [19]. The use of solution precursors and space-confined effects may explain such a high limit of segregation (up to 40%) which is comparable with the best results reported previously [14,21]. The peak widths of the bimetal oxide replicas became broader along with the increase of copper contents, indicating decrease of the average domain size of the oxide crystallites during this process, which was corroborated by calculation using the Scherrer formula (see Table 1). Similar results were reported for catalysts prepared by a reverse microemulsion method [26]. Additionally, the nanocrystalline nature of the oxide frameworks can be identified by the well-resolved diffraction peaks in the wide-angle region of the XRD patterns.

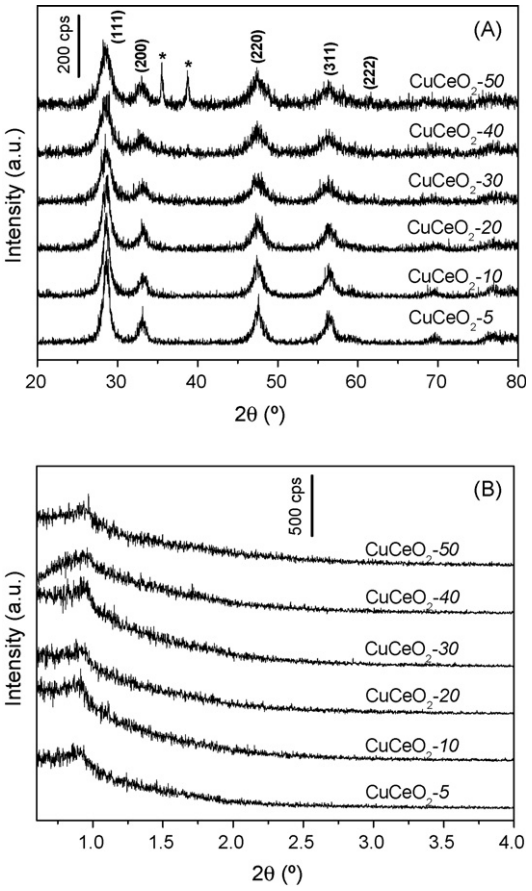

Fig. 1. (A) Wide-angle and (B) low-angle XRD patterns of mesoporous copper cerium bimetal oxide replicas after removal of the KIT-6 silica. The top diffractions in the wide-angle region are indexed using the unit cell of face-centered cubic CeO_2. Asterisks denote the presence of tenorite (CuO).

The low-angle XRD patterns of the bimetal oxide replicas are shown in Fig. 1B. All samples showed the same cubic Ia3d symmetry as their KIT-6 template. The characteristic reflections of (2 1 1) planes at 2θ value of about 0.9° were broad and low in intensity, suggesting the bimetal oxide replicas are less ordered than their silica template, which was often observed for replicas from KIT-6 silica [36,37]. The unit-cell parameters calculated from the positions of the (2 1 1) reflections were about 24.0 nm, which is in fair agreement with the value 24.7 nm for KIT-6 silica (Fig. S1).

3.2. TEM analyses

TEM images are shown in Fig. 2A and B. The ordered arrangement of the oxide nanoparticles can be clearly observed for both $CuCeO_2$-20 and $CuCeO_2$-50 samples. The diameter of the oxide particles in the short dimension is about 9.2 nm, in correspondence with the pore size 10.8 nm of KIT-6 template (Fig. S2). This suggests that the pore channels of the KIT-6 silica confined the growth of the oxide seeds in a limited space and confirms the replication of the bimetal oxide materials from the silica template. Despite the ordered region in the images, the

Table 1
Mean crystallite sizes, BET specific surface areas, total pore volumes and activity data for the mesoporous copper cerium bimetal oxide catalysts

Catalysts	Crystallite size (nm)	BET surface area ($m^2\ g^{-1}$)	Pore volume ($cm^3\ g^{-1}$)	T_{50} (K)	Specific rate at 343 K ($\times 10^{-6}$ $mol_{CO}\ g_{cat}^{-1}\ s^{-1}$)
$CuCeO_2$-5	7.7	116	0.417	432	0.40
$CuCeO_2$-10	7.7	104	0.376	376	1.93
$CuCeO_2$-20	6.4	105	0.355	350	9.18
$CuCeO_2$-30	5.4	108	0.399	360	5.07
$CuCeO_2$-40	5.7	101	0.366	362	4.87
$CuCeO_2$-50	4.9	103	0.355	369	2.45

aggregates of the oxide nanocrystals and large pores among them could be observed, indicating partial collapse of the mesostructures, which probably resulted from the incomplete filling after calcination and thus structural collapse during dissolution of the silica template. HRTEM image of the $CuCeO_2$-20 sample shown in Fig. 2C reveals that the crystalline framework of the replica was assembled by randomly oriented and epitaxially interfaced nanocrystals with clear lattice fringes, all of which have distance of 0.31 ± 0.01 nm, corresponding to the (1 1 1)-spacing of the CeO_2 structure. The sizes of these crystals fall between 3 and 9 nm in agreement with the values estimated by the XRD analyses. No particles of copper oxide were found and the EDX spectra proved the removal of the silica down to trace levels (<1 wt%).

3.3. N_2-sorption analyses

The as-synthesized KIT-6 template showed a type IV isotherm with H1 hysteresis, characteristic of mesoporous materials. They also exhibited large BET specific surface area (500 $m^2\ g^{-1}$) and pore volume (1.26 $cm^3\ g^{-1}$) as well as narrow pore-size distribution centered at 10.1 nm (Fig. S2). N_2-sorption isotherms of the bimetal oxides shown in Fig. 3A are typical for mesoporous transitional-metal oxides prepared via the nanocasting pathway [37–39]. The adsorption jump at $P/P_0 = 0.5$–0.7 and hysteresis are attributed to the capillary condensation in the mesopores; whereas, the uptake at high relative pressure is owing to the existence of large pores among the aggregates based on the TEM analyses. Fig. 3B shows a little wide pore-size distributions with maximum around 3.6 nm, in good agreement with that expected from replicas of the KIT-6 template [37,38]. All the mesoporous bimetal oxide replicas exhibited large BET specific surface areas (>100 $m^2\ g^{-1}$) and pore volumes (>0.35 $cm^3\ g^{-1}$). Moreover, no obvious loss in surface areas or pore volumes was observed when the copper content reached up to 50% (Table 1), in contrast with CuO-loaded mesoporous CeO_2 catalysts reported recently [32], for which, however, the BET specific surface areas depleted by 25% when the copper content increased from 0 to 30%. Compared to the catalysts reported, these mesoporous copper cerium bimetal oxides are prepared in a more simple way and have merits of large surface areas and pore volumes as well as homogeneous dispersion of copper species exactly what desired for many surface catalytic reactions, for example, catalytic CO oxidation.

3.4. XPS analyses

XPS of the core level region of Cu 2p in $CuCeO_2$-X (X = 5, 20, 50) catalysts are shown in Fig. 4A. Accordingly, the Cu($2p_{3/2,\ 1/2}$) peaks at around 934.0 and 953.8 eV with shake-up structure at 940–945 eV in the spectra can only be attributed to Cu(II) ions [18,40]. Weak intensity of the Cu 2p peaks in the spectrum for the $CuCeO_2$-5 catalyst was due to the relatively low copper content. On the other hand, the main Cu ($2p_{3/2,\ 1/2}$) lines became more and more broad and asymmetric with increase of the copper content; signifying different copper species were created during this process and contributed to the line width and asymmetry [9]. The same explanation also holds true for the Ce 3d peak broadening (Fig. 4B). The spectral features at 880–920 eV shown in Fig. 4B correspond to Ce 3d core levels. The two principal peaks for Ce($3d_{5/2,\ 3/2}$) and four satellites marked by asterisks are associated with the Ce(IV) $4f^0$ initial state of CeO_2 [40]. Nevertheless, the characteristic peak of Ce(IV) $3d_{3/2}$ at 916.7 eV for the $CuCeO_2$-50 catalyst became broader and relatively low in intensity, strongly suggesting presence of Ce(III). Concomitant reduction of copper and cerium oxides provided unambiguous evidence of existence of synergistic interaction between copper species and ceria matrices in the mesoporous copper cerium bimetal oxides, which had significant effects on the catalytic activity [10,25]. The surface concentrations of Cu were 4.1 and 16.6 mol%, corresponding to Cu/Ce molar ratios of 0.042 and 0.199, for $CuCeO_2$-5 and $CuCeO_2$-20 catalysts, respectively. The surface concentrations of Cu are a little lower than the nominal percentages for the two catalysts (5 and 20 mol%), indicating a partial encapsulation of copper species by crystalline ceria or preferable location of copper species at boundaries of the CeO_2 crystallites [23]. A reliable Cu/Ce molar ratio of the $CuCeO_2$-50 catalyst was difficult to obtain due to peak broadening and less defined peak width.

3.5. Catalytic performance for CO oxidation

The catalytic activities of the mesoporous copper cerium bimetal oxide catalysts for CO oxidation as a function of reaction temperature are shown in Fig. 5. The effects of copper concentration on the activities of the above catalysts can be clearly observed. The $CuCeO_2$-20 catalyst exhibited the highest activity for catalytic CO oxidation with the lowest T_{50} at 350 K. The catalysts with lower copper content suffered a substantial

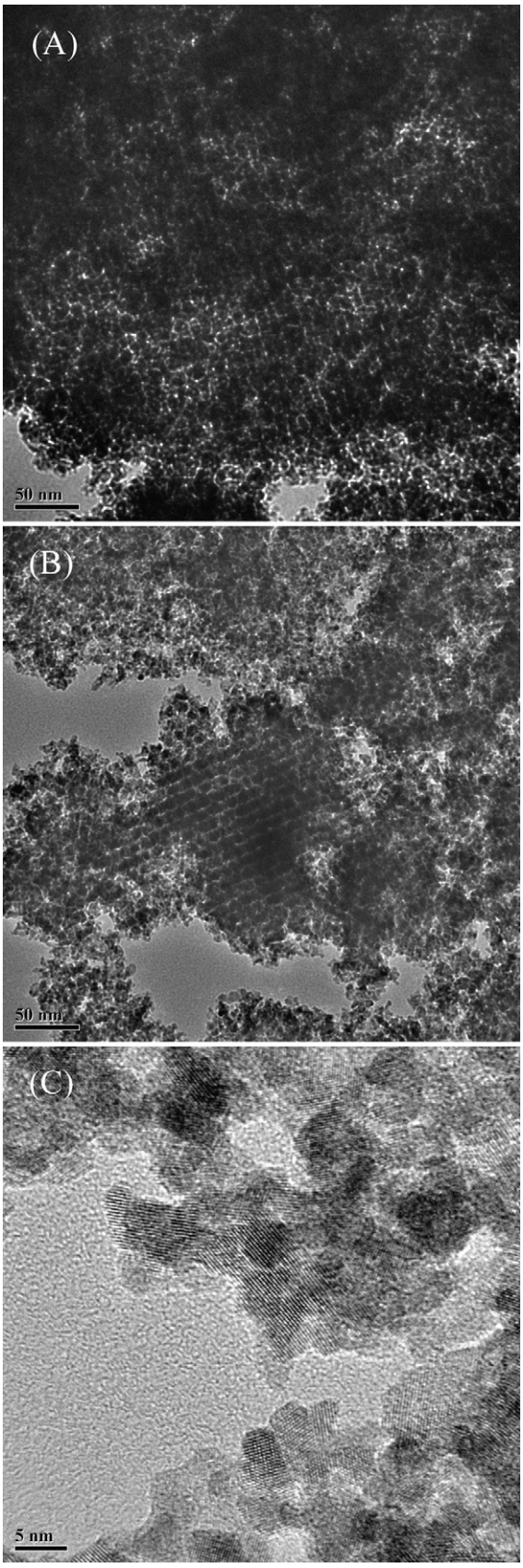

Fig. 2. TEM images of template-free mesoporous copper cerium bimetal oxides with (A) 20%, (B) 50% copper contents and (C) high-resolution TEM of mesoporous $CuCeO_2$-20 replica.

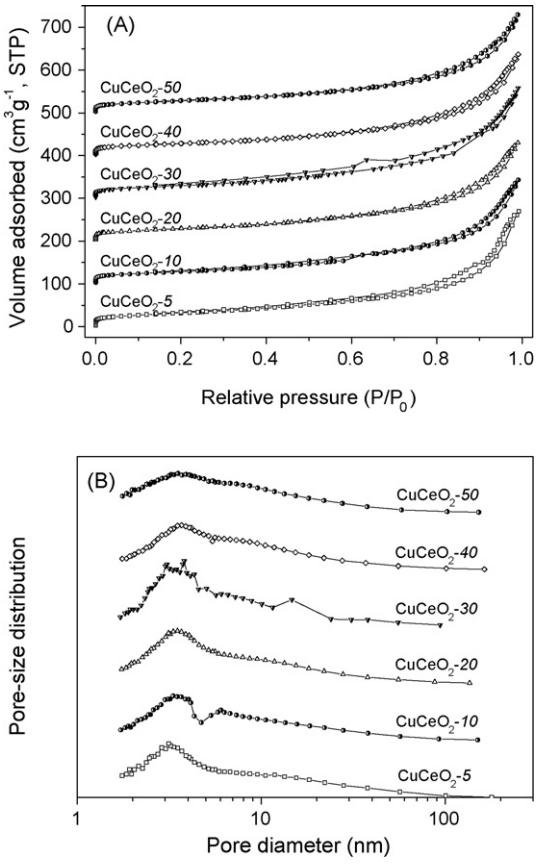

Fig. 3. (A) Nitrogen-sorption isotherms and (B) pore-size distribution curves of mesoporous copper cerium bimetal oxide materials. Each isotherm is offset along the *y*-axis by 100 $cm^3\ g^{-1}$ relative to the previous one.

loss in activity. At T_{50} of the $CuCeO_2$-20 catalyst, only 3 and 10% CO conversion were achieved for the $CuCeO_2$-5 and -10 catalysts, respectively. When the copper content exceeded 20%, the catalytic activity decreased slowly and T_{50} increased 10, 12, and 19 K over the catalysts with 30, 40 and 50% copper contents, respectively. The specific rate data also corroborated the activity sequence of the bimetal oxide catalysts. Table 1 summarized the T_{50} and specific rates at 343 K for all the mesoporous bimetal oxide catalysts as well as corresponding structural and textural parameters. The observed concentration effect suggests that 20% seems to be near the optimum concentration of copper allowed using the nanocasting pathway to achieve good dispersion of the copper species on the ceria matrices in this case. As to the catalysts with low copper contents (<20 mol%), the surface copper species are unsaturated, thus the catalytic results are closely related to the concentration of copper contents due to the limited active sites homogeneously distributed on the catalyst surfaces and weak interaction between copper species and ceria matrices. The less of the copper contents are, the less of the active sites distributed on the catalyst surfaces and the weaker the interaction between copper species and ceria matrices will be. Here, the smaller sizes of the crystalline ceria, which decreased a little along with the increase of the copper contents, are also more beneficial for the interaction between copper species and ceria matrices. For the catalysts with copper contents beyond the proper quantity

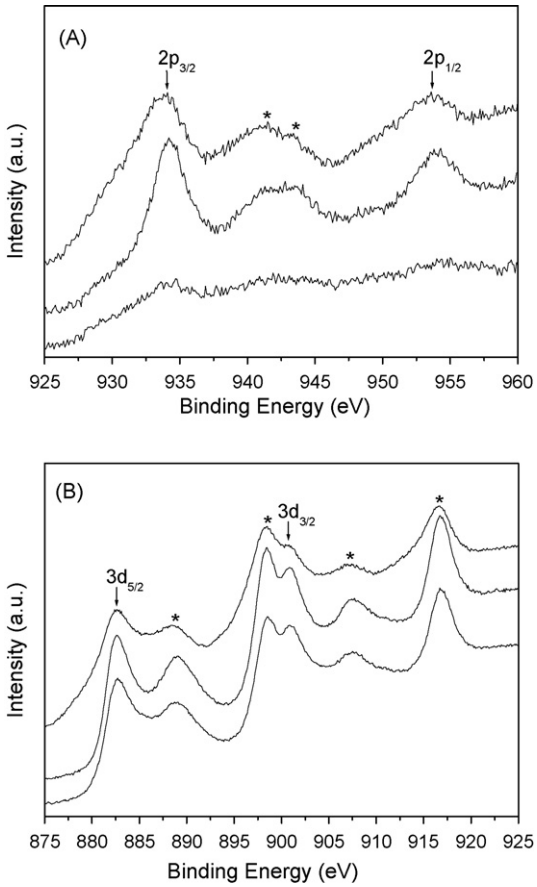

Fig. 4. XPS of core level region of (A) Cu 2p and (B) Ce 3d obtained on mesoporous copper cerium bimetal oxides with 5% (bottom), 20% (middle) and 50% (top) copper contents. Asterisks denote positions of the satellites.

(20 mol%), the excessive copper species will aggregate due to oversaturation of the surface copper species and a second phase tenorite formed based on the XRD analyses. The formation of tenorite on the catalyst surfaces may be unfavorable for catalytic CO oxidation. Even though, the smaller sizes of the crystalline ceria could be observed (Table 1) along with the increase of the copper contents of the samples, which may result in a little stronger interaction between copper species and ceria matrices, the decreased activity tendency cannot be avoided because of the dominant effect of the formation of tenorite. The more copper contents are incorporated, the more amounts of tenorite will form, thus, the poorer catalytic activity the catalyst will exhibit. So, when copper contents reach an optimum concentration 20 mol% in our work, the catalyst has the maximum of active sites on the surfaces and a certain strong interaction between copper species and ceria matrices. Similar reports can also be found in the $CuO–CeO_2$ catalysts prepared by various methods for the selective oxidation of CO in the presence of excess H_2, CO_2 or H_2O [14,20].

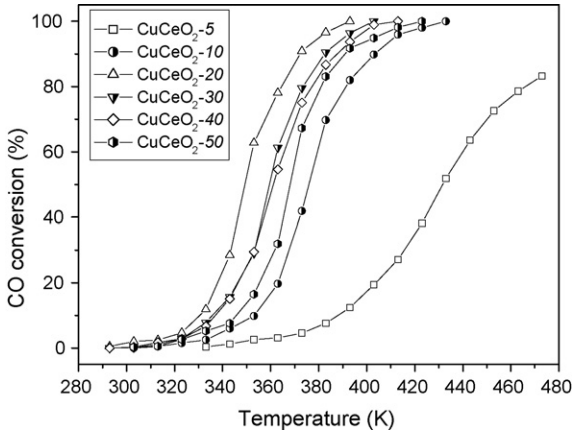

Fig. 5. CO conversion as a function of reaction temperature for mesoporous copper cerium bimetal oxide catalysts.

The catalytic stability for CO oxidation was further investigated over the most active catalyst, namely the $CuCeO_2$-20 catalyst. The conversion decay curve for the $CuCeO_2$-20 catalyst is shown in Fig. S3. Less than 2% loss of CO conversion was observed after 10 h on stream at 373 K, demonstrating robust long-term stability of the catalyst. Moreover, the $CuCeO_2$-20 catalyst showed excellent recycling stability for three runs of CO oxidation (Fig. S4).

The catalytic activity and stability exhibited by the mesoporous $CuCeO_2$-20 catalyst are comparable or even superior to that reported in previous literatures; especially taking account of the relatively high space velocity of 260,000 mL h^{-1} $g_{cat}{}^{-1}$ used in CO oxidation experiments [10,11,31,32]. In the case of mesoporous ceria supported copper oxides which was incorporated by impregnation technique, although a relatively low space velocity of 20,000 mL h^{-1} $g_{cat}{}^{-1}$ with the volume ratio of the gas mixture $CO:O_2$:He = 1:5:44 was used, the lowest T_{50} (389 K) achieved by the catalyst with 20 mol% copper content was still 39 K higher than that of the catalyst with the same copper content presented in this work, demonstrating the prominent effects of preparation methods on the structural and textural parameters (e.g., degree of copper dispersion, specific surface area and pore volume) and as a result on the catalytic activities of the finally obtained catalyst materials [32]. It was reported that CuO loaded ceria nanorods predominantly exposed more reactive (0 0 1) and (1 1 0) planes showed significant enhancement of the catalytic activity for CO oxidation compared to CuO loaded ceria nanoparticles. The $CuCeO_2$-20 catalyst reported here exhibited even higher catalytic activity with the temperature of complete CO conversion about 30 K lower than that of the CuO loaded ceria nanorods (423 K) under an unfavorable conditions for CO oxidation (higher space velocity and less catalyst mass) [31]. The parallel experiments have substantiated the activity enhancement of the $CuCeO_2$-20 catalyst compared with 20 mol% CuO-loaded mesoporous CeO_2. Fig. S5 shows the light-off curves of the above two catalysts under conditions used in this work. It can be seen clearly that the curve of the CuO-loaded CeO_2 shift to high-temperature range with T_{50} of 405 K, more than 50 K higher than that of the $CuCeO_2$-20 catalyst. Under similar catalytic conditions used for the series of CuO-loaded mesoporous CeO_2 [32], the light-off curve of the 20 mol% CuO-loaded CeO_2 is similar to that of the CuO-loaded CeO_2 with a little higher T_{50} (Fig. S6).

The excellent catalytic performance of $CuCeO_2$-X (X = 5–50) is associated with the novel structural and textural characteristics

of the mesoporous copper cerium bimetal oxides synthesized via the nanocasting route. First, large surface area is favorable for catalytic activity enhancement due to its ability to offer more sites for active species (i.e., low-coordinated copper ion clusters) to anchor on. Second, the unique pore structures with interconnected pore channels and volumes make it easier for the reactants to access the surface active sites therefore facilitate the CO adsorption and oxidation on the active sites as well as the product desorption. Last but not the least, the combination of using mixed solutions as metal sources and space-confined effects realized that copper species highly dispersed on the ceria matrices based on the wide-angle XRD analyses. The intimate contact between the copper species and ceria matrices enhanced the synergistic interactions and redox properties between catalysts and supports, which also strongly suggests that the interfacial region is the catalytic active site for CO oxidation [25,32].

When the $CuCeO_2$-20 catalyst was calcined in static air at 873 K for 6 h, the catalytic activity of these bimetal oxides for CO oxidation was still high with T_{50} for the calcined $CuCeO_2$-20 catalyst only 6 K higher than that for the as-prepared one (Fig. S7), which is due to the preserved high degree of copper dispersion (Fig. S8), although the BET surface area of the calcined catalyst decreased by 50% because of formation of large particles (Fig. S9).

4. Conclusion

Nanocasting method using KIT-6 silica as hard template was employed to prepare mesoporous copper cerium bimetal oxides in a wide range of compositions. No tenorite segregation was detected until the copper content reach up to 40%. The mixed oxide replicas exhibited large specific surface areas and pore volumes which were independent of the copper content in the bimetal oxides. X-ray photoelectron spectra indicate that copper and cerium species on the catalyst surface were predominantly in the Cu(II) and Ce(IV) oxidation states, respectively. The catalysts reported in this work showed comparable or even superior activities to literature data for catalytic CO oxidation. The excellent catalytic performance is associated with the structural and textural characteristics of large surface area, pore structures with interconnected pore channels and volumes as well as highly dispersed copper species on the ceria matrices. 20 mol% is the optimum concentration of copper to achieve the best catalytic performance in this case. More copper species homogeneously dispersed on the porous ceria matrices with larger surface area and more suitable pore size will be the focus to improve the catalytic activities in the catalytic CO oxidation.

Acknowledgements

The authors gratefully thank the financial support by Chinese National Science Foundation (No. U0734002), Chinese Academy of Sciences (Bairen Project and Creative Foundation), and Shanghai Nanotechnology Promotion Center (No. 0652nm025).

Appendix A. Supplementary data

Supplementary data associated with this article can be found, in the online version, at doi:10.1016/j.apcatb.2007.12.017.

References

[1] B. Wen, M. He, Appl. Catal. B: Environ. 37 (2002) 75.
[2] J. Papavasiliou, G. Avgouropoulos, T. Ioannides, Appl. Catal. B: Environ. 66 (2006) 168.
[3] B. Srinivasan, S.D. Gardner, Surf. Interface Anal. 26 (1998) 1035.
[4] F. Mariño, C. Descorme, D. Duprez, Appl. Catal. B: Environ. 58 (2005) 175.
[5] W. Liu, M. Flytzani-Stephanopoulos, J. Catal. 153 (1995) 304.
[6] J.B. Wang, D.H. Tsai, T.J. Huang, J. Catal. 208 (2002) 370.
[7] X. Wang, J.A. Rodriguez, J.C. Hanson, D. Gamarra, A. Martínez-Arias, M. Fernández-García, J. Phys. Chem. B 110 (2006) 428.
[8] P. Bera, S. Mitra, S. Sampath, M.S. Hedge, Chem. Commun. (2001) 927.
[9] A. Martínez-Arias, M. Fernández-García, J. Soria, J.C. Conesa, J. Catal. 182 (1999) 367.
[10] P.G. Harrison, I.K. Ball, W. Azelee, W. Daniell, D. Goldfarb, Chem. Mater. 12 (2000) 3715.
[11] B. Skårman, D. Grandjean, R.E. Benfield, A. Hinz, A. Andersson, L.R. Wallenberg, J. Catal. 211 (2002) 119.
[12] W. Liu, M. Flytzani-Stephanopoulos, J. Catal. 153 (1995) 317.
[13] Y. Liu, T. Hayakawa, K. Suzuki, S. Hamakawa, T. Tsunoda, T. Ishii, M. Kumagai, Appl. Catal. A: Gen. 223 (2002) 137.
[14] M. Jobbágy, F. Mariño, B. Schonbröd, G. Baronetti, M. Laborde, Chem. Mater. 18 (2006) 1945.
[15] A. Tschöpe, J. Markmann, P. Zimmer, R. Birringer, Chem. Mater. 17 (2005) 3935.
[16] Y. Li, Q. Fu, M. Flytzani-Stephanopoulos, Appl. Catal. B: Environ. 27 (2000) 179.
[17] X. Qi, M. Flytzani-Stephanopoulos, Ind. Eng. Chem. Res. 43 (2004) 3055.
[18] P. Bera, K.R. Priolkar, P.R. Sarode, M.S. Hegde, S. Emura, R. Kumashiro, N.P. Lalla, Chem. Mater. 14 (2002) 3591.
[19] J. Papavasiliou, G. Avgouropoulos, T. Ioannides, Appl. Catal. B: Environ. 69 (2007) 226.
[20] G. Avgouropoulos, T. Ioannides, H. Matralis, Appl. Catal. B: Environ. 56 (2005) 87.
[21] G.R. Rao, H.R. Sahu, B.G. Mishra, Colloids Surf. A: Physicochem. Eng. Aspects 220 (2003) 261.
[22] W. Shan, W. Shen, C. Li, Chem. Mater. 15 (2003) 4761.
[23] B. Skårman, T. Nakayama, D. Grandjean, R.E. Benfield, E. Olsson, K. Niihara, L.R. Wallenberg, Chem. Mater. 14 (2002) 3686.
[24] A. Martínez-Arias, M. Fernández-García, A.B. Hungría, A. Iglesias-Juez, O. Galvez, J.A. Anderson, J.C. Conesa, J. Soria, G. Munuera, J. Catal. 214 (2003) 261.
[25] A. Martínez-Arias, A.B. Hungría, M. Fernández-García, J.C. Conesa, G. Munuera, J. Phys. Chem. B 108 (2004) 17983.
[26] X. Wang, J.A. Rodriguez, J.C. Hanson, D. Gamarra, A. Martínez-Arias, M. Fernández-García, J. Phys. Chem. B 109 (2005) 19595.
[27] G. Sedmak, S. Hočevar, J. Levec, J. Catal. 222 (2004) 87.
[28] E. Moretti, M. Lenarda, L. Storaro, A. Talon, R. Frattini, S. Polizzi, E. Rodríguez-Castellón, A. Jiménez-López, Appl. Catal. B: Environ. 72 (2007) 149.
[29] H. Kušar, S. Hočevar, J. Levec, Appl. Catal. B: Environ. 63 (2006) 194.
[30] F. Huber, Z. Yu, J.C. Walmsley, D. Chen, H.J. Venvik, A. Holmen, Appl. Catal. B: Environ. 71 (2007) 7.
[31] K. Zhou, R. Xu, X. Sun, H. Chen, Q. Tian, D. Shen, Y. Li, Catal. Lett. 101 (2005) 169.
[32] W. Shen, X. Dong, Y. Zhu, H. Chen, J. Shi, Micropor. Mesopor. Mater. 85 (2005) 157.
[33] K. Zhou, R. Wang, B. Xu, Y. Li, Nanotechnology 17 (2006) 3939.
[34] L. Gou, C.J. Murphy, Chem. Commun. (2005) 5907.

[35] F. Kleitz, S.H. Choi, R. Ryoo, Chem. Commun. (2003) 2136.
[36] E. Rossinyol, J. Arbiol, F. Peiró, A. Cornet, J.R. Morante, B. Tian, T. Bo, D. Zhao, Sens. Actuators B: Chem. 109 (2005) 57.
[37] F. Jiao, K.M. Shaju, P.G. Bruce, Angew. Chem. Int. Ed. 44 (2005) 6550.
[38] F. Jiao, J.C. Jumas, M. Womes, A.V. Chadwick, A. Harrison, P.G. Bruce, J. Am. Chem. Soc. 128 (2006) 12905.
[39] F. Jiao, A. Harrison, J.C. Jumas, A.V. Chadwick, W. Kockelmann, P.G. Bruce, J. Am. Chem. Soc. 128 (2006) 5468.
[40] A. Tschöpe, M.L. Trudeau, J.Y. Ying, J. Phys. Chem. B 103 (1999) 8858.